Supplement: A new spin on LIGO-Virgo binary black holes

Sylvia Biscoveanu,[1,2,*] Maximiliano Isi,[1,2,†] Salvatore Vitale,[1,2] and Vijay Varma[3,4,‡]

[1] *LIGO Laboratory, Massachusetts Institute of Technology, Cambridge, Massachusetts 02139, USA*
[2] *Department of Physics and Kavli Institute for Astrophysics and Space Research, Massachusetts Institute of Technology, 77 Massachusetts Ave, Cambridge, MA 02139, USA*
[3] *TAPIR, California Institute of Technology, Pasadena, CA 91125, USA*
[4] *Department of Physics, and Cornell Center for Astrophysics and Planetary Science, Cornell University, Ithaca, New York 14853, USA*

(Dated: March 18, 2021)

Parameter estimation methods

To analyze the simulated signals, we perform Bayesian parameter estimation using the standard Gaussian likelihood for gravitational-wave data [1, 2]:

$$\mathcal{L}(d_i|\theta) = \prod_j \frac{2}{\pi T S_n(f_j)} \exp\left[-\frac{2|d_i(f_j) - h(f_j;\theta)|^2}{T S_n(f_j)}\right], \tag{1}$$

where T is the duration of the data segment being analyzed, $S_n(f_j)$ is the noise power spectral density of the detector, $d_i(f_j)$ is the strain data for event i, and $h(f_j;\theta)$ is the waveform model for the compact binary source. We simulate the measurement using the `LALInference` algorithm [2] and the numerical relativity surrogate waveform model NRSur7dq4 [3]. In order to obtain posterior samples for the parameters θ using the likelihood in Eq. 1, we impose priors that are uniform in the component masses m_1, m_2 between 10 $M_\odot$ and 240 $M_\odot$, with constraints on the total mass between 70 $M_\odot$ and 240 $M_\odot$ and on mass ratio q between 0.2 and 1. The luminosity distance prior is $\propto d_L^2$ over the range 1–7000 Mpc.

For the spin tilt population inference, we simultaneously fit the mass and spin magnitude distributions. We follow [4, 5] and assume that both of the black hole (BH) spin magnitudes under the mass sorting are drawn from the same Beta distribution with hyperparameters α and β,

$$p(\chi_{1/2}|\alpha,\beta) = \frac{\chi_{1/2}^{\alpha-1}(1-\chi_{1/2})^{\beta-1}}{B(\alpha,\beta)}, \tag{2}$$

where $B(\alpha,\beta)$ is the Beta function. We restrict the priors on the Beta function parameters to exclude values of $\alpha,\beta \leq 1$ corresponding to singular Beta distributions. This means that $p(\chi)$ *must* peak within $0 < \chi < 1$, as nonsingular Beta distributions vanish at those values. The Beta distribution described in Eq. 2 can also be parameterized in terms of its mean and variance:

$$\mu(\chi) = \frac{\alpha}{\alpha+\beta}, \tag{3}$$

$$\sigma^2(\chi) = \frac{\alpha\beta}{(\alpha+\beta)^2(\alpha+\beta+1)}. \tag{4}$$

We choose to sample in $\mu(\chi)$ and $\sigma^2(\chi)$, imposing constraints such that $\alpha,\beta > 1$ to restrict the parameter space to only nonsingular Beta distributions.

The distributions for χ_A and χ_B obtained by applying order statistics to the Beta distribution for $\chi_{1/2}$ are given by:

$$p(\chi_A) = 2\,p(\chi_{1/2}|\alpha,\beta)\,\mathrm{CDF}(\chi_{1/2}|\alpha,\beta)\,, \tag{5}$$

$$p(\chi_B) = 2\,p(\chi_{1/2}|\alpha,\beta)\left[1-\mathrm{CDF}(\chi_{1/2}|\alpha,\beta)\right], \tag{6}$$

assuming χ_A is the maximum and χ_B is the minimum of two draws from $p(\chi_{1/2}|\alpha,\beta)$. $\mathrm{CDF}(\chi_{1/2})$ is the cumulative distribution function for $\chi_{1/2}$ given by the regularized incomplete Beta function with parameters (α,β).

We further assume that the primary mass distribution is described by the sum of a truncated power-law with low-mass smoothing and a Gaussian component [6]. The hyperparameters describing this model are the slope α_m, upper and lower cutoffs $m_{\max}$ and $m_{\min}$, the low-mass smoothing parameter δ_m, the peak and width of the Gaussian component μ_m and σ_m, and the mixing fraction between the two components λ_{peak}. The mass ratio distribution is modeled as a power law with slope β_q. This corresponds to Model C from [5], dubbed "power-law + peak". We use this same mass model when computing the spin magnitude distribution using prior samples for the GWTC-2 events, shown in the dashed black line in Fig. 3 in the main text.

Following [7], the distribution for spin tilt angles is given by the sum of an isotropic component and a preferentially aligned component, which is composed of the product of two truncated Gaussians peaked at $\cos t_i = 1$ for each tilt angle:

$$p(\cos t_{1/A}, \cos t_{2/B}|\sigma_{1/A},\sigma_{2/B},\xi) = \frac{1-\xi}{4} + \frac{2\xi}{\pi}\prod_{i\in\{1/A,2/B\}}\frac{\exp(-(1-\cos t_i)^2/(2\sigma_i^2))}{\sigma_i \mathrm{erf}(\sqrt{2}/\sigma_i)}, \tag{7}$$

where the hyperparameter ξ gives the mixture fraction between the two components. The complete population model, $\pi(\theta|\Lambda)$, is given by the product of Eqs. 2, 7, and the "power-law + peak" mass distribution.

Using the population model $\pi(\theta|\Lambda)$ to describe the distribution of individual-event parameters θ, the likelihood

of observing the hierarchical parameters Λ for a data set $\{d\}$ consisting of $N_{\rm det}$ detected events is given by:

$$\mathcal{L}(\{d\}|\Lambda) \propto \prod_{i=1}^{N_{\rm det}} \frac{\int \mathcal{L}(d_i|\theta)\pi(\theta|\Lambda)}{\alpha(\Lambda)} \tag{8}$$

where $\alpha(\Lambda)$ represents the detectable fraction of events assuming the individual-event parameters are drawn from distributions specified by hyperparameters Λ [8–13]. We use the sensitive spacetime volume estimates released by the LVC in [14], which for the GWTC-2 analysis were determined through injection campaign [15] and for the GWTC-1 events were obtained using simulated data. We calculate $\alpha(\Lambda)$ using the formalism described in [16]. We do not account for the selection biases due to the spin parameters, since those have a much smaller effect than the mass parameters [17].

The likelihood in Eq. 8 is evaluated using a Monte Carlo integral over the individual-event parameter posteriors released by the LVC for the binary BH (BBH) events included in GWTC-1 [18, 19] and GWTC-2 [15, 20]. For the GWTC-1 events, we use the samples obtained with the IMRPhenomPv2 waveform model, while for GWTC-2 we use the "Publication" posterior samples presented in [15], which in most cases use a combination of waveform models including the effects of spin precession and higher-order multipoles. For GWTC-2, we only analyze the 44 confident BBH detections with a false alarm rate < 1 yr^{-1} and exclude the events where at least one of the compact objects has considerable posterior support below 3 $M_\odot$. We use the `dynesty` [21] sampler, as implemented in the `GWPopulation` [22] package, to obtain hyperparameter posterior samples.

The posterior population distribution calculated using the hyperparameter posteriors obtained using the likelihood in Eq. 8 is given by:

$$\mathrm{PPD}(\theta|\{d\}) = \int \pi(\theta|\Lambda)p(\Lambda|\{d\})d\Lambda. \tag{9}$$

The priors and posterior results for all hyperparameters except $\sigma_{1/A}$ and $\sigma_{2/B}$ for the spin-sorted tilt inference performed using the GWTC-2 BBH events are shown in Table I. The priors are uniform for all parameters and identical for both the mass and spin-sorted tilt analysis. We use uniform priors over the range $(0, 4)$ for the tilt σ parameters. The posterior for the spin tilt mixing fraction ξ peaks at the upper edge of its prior, indicating that a purely isotropic distribution of tilts is statistically disfavored by the data. We obtain posteriors for the mass, spin magnitude, and ξ hyperparameters comparable to those quoted in [17]. The results for these parameters change negligibly under the mass and spin sortings.

The corner plot of the tilt σ hyperparameters for the GWTC-1 analysis is shown in Fig. 1. Even with only the GWTC-1 events, the corner of parameter space at $\sigma_{1/A} = \sigma_{2/B} = 0$ representing a fully-aligned population is excluded at $> 90\%$ credibility for both the mass and spin sortings. The posterior for σ_B is less constrained than that for σ_2—indicating that for this analysis, the information on the tilt angles at the population level is predominantly obtained from the measurement of the highest spinning object, rather than the most massive. A similar trend is present in the σ posteriors for the full GWTC-2 analysis shown in Fig. 4 in the main text.

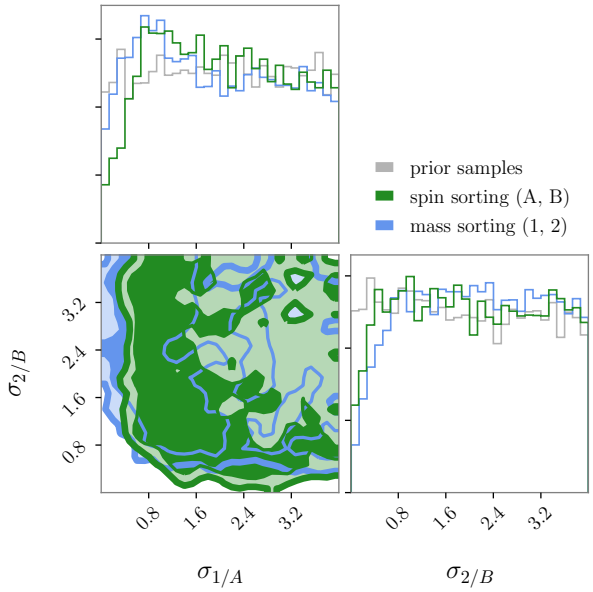

FIG. 1. Corner plot comparing the inference on the spin tilt hyperparameters using the mass sorted tilts θ_1 and θ_2 and spin sorted tilts θ_A and θ_B for the GWTC-1 events. The posteriors obtained using prior samples for the individual events are shown in grey.

Additional results for individual sources

For certain sources, we note significant differences in the posteriors obtained with the two different waveform models applied to BBHs in GWTC-1: IMRPhenomPv2 [23–25], which uses an effective precessing spin model, and SEOBNRv3, which uses a fully precessing spin model [26–28]. For GW150914, the one-dimensional posterior for χ_A is much more tightly constrained for SEOBNRv3, with $\chi_A = 0.39^{+0.44}_{-0.24}$ compared to $\chi_A = 0.49^{+0.45}_{-0.38}$ for IMRPhenomPv2, a feature which is not as easily recognizable in the χ_1 posterior. A comparison of the spin magnitudes obtained using both waveform models is shown in Fig. 2. Similarly for GW170814, the posterior for χ_A turns over at around $\chi_A \sim 0.5$ for SEOBNRv3, but not for IMRPhenomPv2 (Fig. 3). The two-dimensional χ_A, χ_B posterior recovered with SEOBNRv3 is much more tightly clustered around low spins for GW170814 and also for GW170818,

Parameter	Prior	GWTC-1	GWTC-2
α_m	U(-4, 12)	$6.41^{+4.87}_{-4.44}$	$2.96^{+0.77}_{-0.63}$
β_m	U(-4, 12)	$5.60^{+5.65}_{-5.73}$	$1.01^{+2.26}_{-1.41}$
$m_{\rm max}$	U(30 $M_\odot$, 100 $M_\odot$)	$59.80^{+35.92}_{-26.66}$ $M_\odot$	$86.30^{+12.10}_{-12.66}$ $M_\odot$
$m_{\rm min}$	U(2 $M_\odot$, 10 $M_\odot$)	$7.40^{+1.35}_{-3.31}$ $M_\odot$	$4.71^{+1.38}_{-1.84}$ $M_\odot$
δ_m	U(0 $M_\odot$, 10 $M_\odot$)	$2.58^{+5.28}_{-2.38}$ $M_\odot$	$4.59^{+4.24.35}_{-3.98}$ $M_\odot$
μ_m	U(20 $M_\odot$, 50 $M_\odot$)	$28.60^{+5.71}_{-6.98}$ $M_\odot$	$32.42^{+3.52}_{-5.91}$ $M_\odot$
σ_m	U(0.4 $M_\odot$, 10 $M_\odot$)	$6.13^{+3.37}_{-4.18}$ $M_\odot$	$5.17^{+4.21}_{-3.85}$ $M_\odot$
$\lambda_{\rm peak}$	U(0, 1)	$0.19^{+0.40}_{-0.16}$	$0.07^{+0.13}_{-0.05}$
$\mu(\chi)$	U(0, 1)	$0.30^{+0.20}_{-0.15}$	$0.31^{+0.11}_{-0.09}$
$\sigma^2(\chi)$	U(0, 0.25)	$0.02^{+0.03}_{-0.02}$	$0.03^{+0.02}_{-0.02}$
ξ	U(0, 1)	$0.54^{+0.41}_{-0.47}$	$0.79^{+0.19}_{-0.43}$

TABLE I. Priors, posterior medians, and 90% credible intervals for the hyperparameters used in our population analysis obtained for spin-sorted component tilt angles including both GWTC-1 events alone and the 44 confident BBH detections in GWTC-2. All the priors are uniform across the specified range and match those used in [17].

although these features are distinguishable in the χ_1, χ_2 posteriors as well.

For the unequal-mass binary GW190412 [29], the spin sorting introduces degeneracies in the spin parameters that were not present in the mass-based sorting. The one-dimensional χ_A posterior is much less constrained than χ_1, and it features a tail extending to higher spin magnitudes. Unlike for the other BBH signals, which are consistent with $q = 1$, the tilt posteriors for this event change considerably between the mass and spin sortings. There is a clear degeneracy observed between θ_A and θ_B where either one or the other is constrained to lie in the orbital plane, similar to the pattern observed for θ_1 and θ_2 in our simulated signal. The χ_B posterior is more constrained than the χ_2 posterior, peaking at $\chi_B \sim 0.5$ and ruling out $\chi_B \gtrsim 0.7$ with 3σ credibility across the various waveforms allowing spin precession. Fig. 4 compares the posteriors on the spin magnitudes and tilts for both the spin and mass sorting obtained using a waveform model that allows for spin precession. Based on the application of the spin sorting to this event, we conclude that it is preferable to use the mass sorting when the mass ratio of the binary can be clearly constrained away from equal mass, as expected from our simulations.

When analyzing the posteriors obtained for GW190412 with aligned-spin waveforms, the χ_1, χ_2 posterior shown in Fig. 5 exhibits a strong correlation depending on orientation with respect to $\vec{L}$: high, aligned primary spins are allowed when the secondary spin is high and anti-aligned; low, aligned primary spins are allowed when the secondary spin is high and aligned. This correlation, which is due to the strong constraint on the effective aligned spin, $\chi_{\rm eff}$, is simply reflected over the $\chi_A = \chi_B$ boundary when the posteriors are projected into the spin sorting.

For the binary NSs, GW170817 [30] and GW190425 [31], two priors were used to include or exclude high spins (maximum χ_i of 0.99 vs 0.05, respectively), where the high-spin prior allows for the possibility that the binary components are BHs. For the high-spin prior, the posteriors for both $\chi_{1/A}$ and $\chi_{2/B}$ favor low spin values for both events and for both aligned and precessing-spin waveforms. The posteriors for the spin magnitudes are less informative for the low-spin prior, since the prior volume is considerably reduced. For GW190425, we find that the constraints on $\cos\theta_A$ are tighter than those on $\cos\theta_1$ for the precessing-spin waveform IMRPhenomPv2_NRTidal: $\cos\theta_A = 0.24^{+0.60}_{-0.44}$ compared to $\cos\theta_1 = 0.24^{+0.62}_{-0.65}$ for the high-spin prior, with a similar trend for the low-spin prior. Conversely, the posterior for $\cos\theta_B$ broadens slightly compared to that of $\cos\theta_2$, consistent with the behavior observed for the simulated signal.

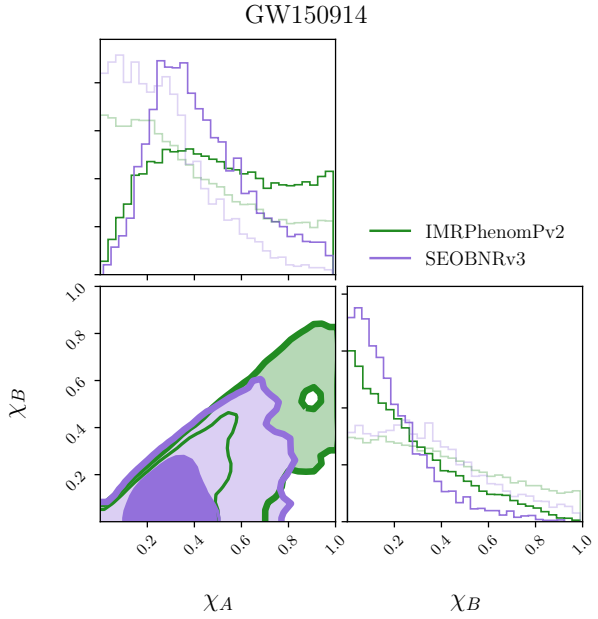

FIG. 2. Comparison corner plot for the spin magnitudes for the posteriors obtained using both the IMRPhenomPv2 (green) and SEOBNRv3 (purple) waveforms for GW150914 using the spin sorting. The marginalized posteriors obtained using the mass sorting are shown in lighter green and purple.

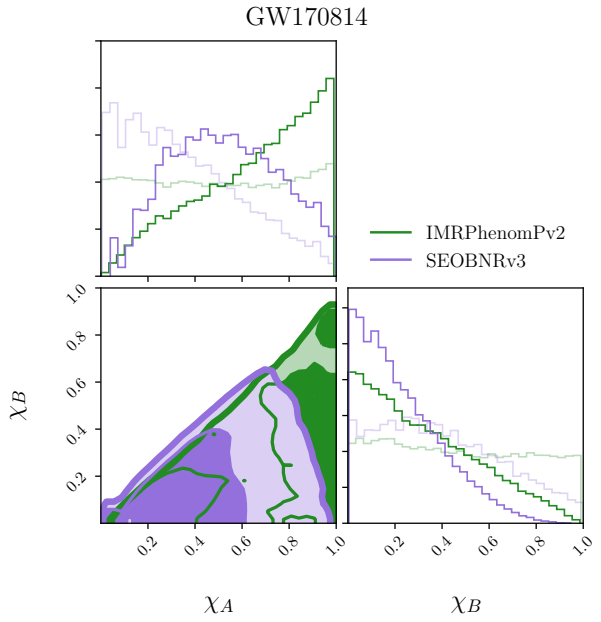

FIG. 3. Comparison corner plot for the spin magnitudes for the posteriors obtained using both the IMRPhenomPv2 (green) and SEOBNRv3 (purple) waveforms for GW170814 using the spin sorting. The marginalized posteriors obtained using the mass sorting are shown in lighter green and purple.

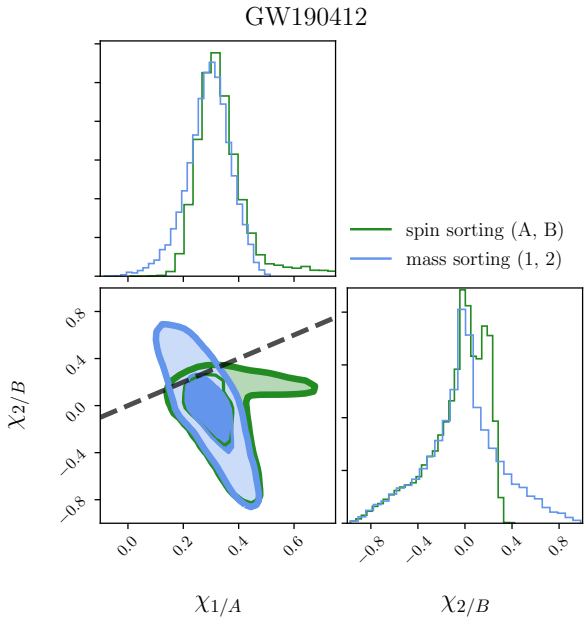

FIG. 5. Comparison corner plot for the spin magnitudes for the posteriors obtained using the aligned-spin waveform SEOBNRv4HM_ROM for GW190412 using both the spin (green) and mass (blue) sorting. Negative values of χ are included due to anti-alignment.

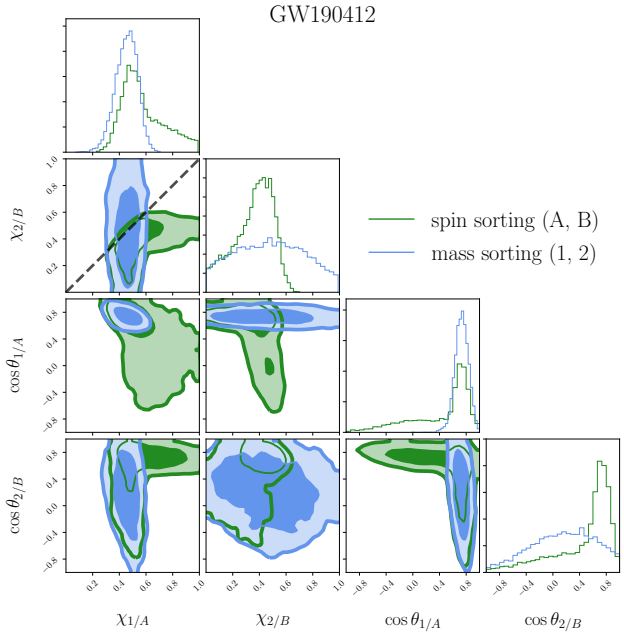

FIG. 4. Comparison corner plot for the spin magnitudes and tilts for the posteriors obtained using the SEOBNRv4PHM waveform for GW190412.

Spin disk plots

In Figs. 6–9, we show the spin disk plots for the spin-sorted posterior samples for the first 13 LVC detections (see e.g. Fig. 5 of [32]) calculated using `PESummary` [33]. The angular direction indicates the misalignment with the orbital angular momentum, while the radial direction shows the spin magnitude for the highest-spinning compact object on the left and the least-spinning object on the right. We show the posterior samples obtained using the IMRPhenomPv2 waveform for BBH events reported in GWTC-1, IMRPhenomPv2_NRTidal with the high-spin prior for the two BNS detections, and IMRPhenomPv3 for GW190412. We also show the disk plots for the posteriors obtained with the SEOBNRv3 waveform for GW150914 and GW170814 in Figs. 6 and 8 to supplement the comparison in Figs. 2 and 3.

* sbisco@mit.edu
† NHFP Einstein fellow
‡ Klarman fellow

[1] J. D. Romano and N. J. Cornish, Living Rev. Rel. **20**, 2 (2017), arXiv:1608.06889 [gr-qc].
[2] J. Veitch *et al.*, Phys. Rev. **D91**, 042003 (2015), arXiv:1409.7215 [gr-qc].

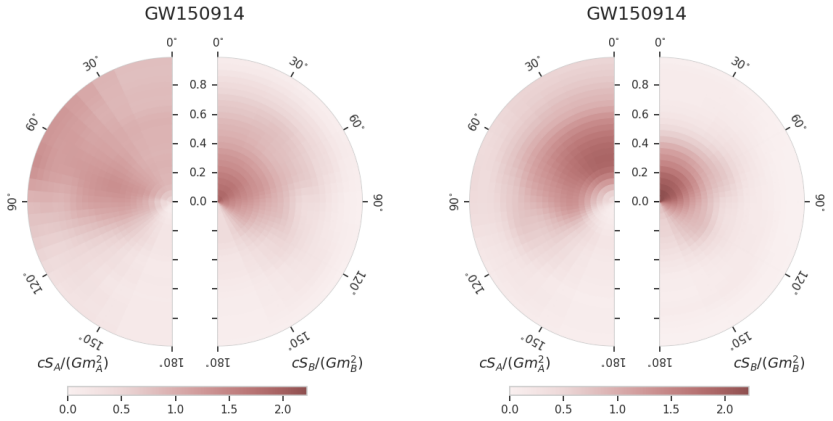

FIG. 6. Spin disk plots for the spin-sorted posterior samples for GW150914 using the IMRPhenomPv2 waveform on the left and the SEOBNRv3 waveform on the right.

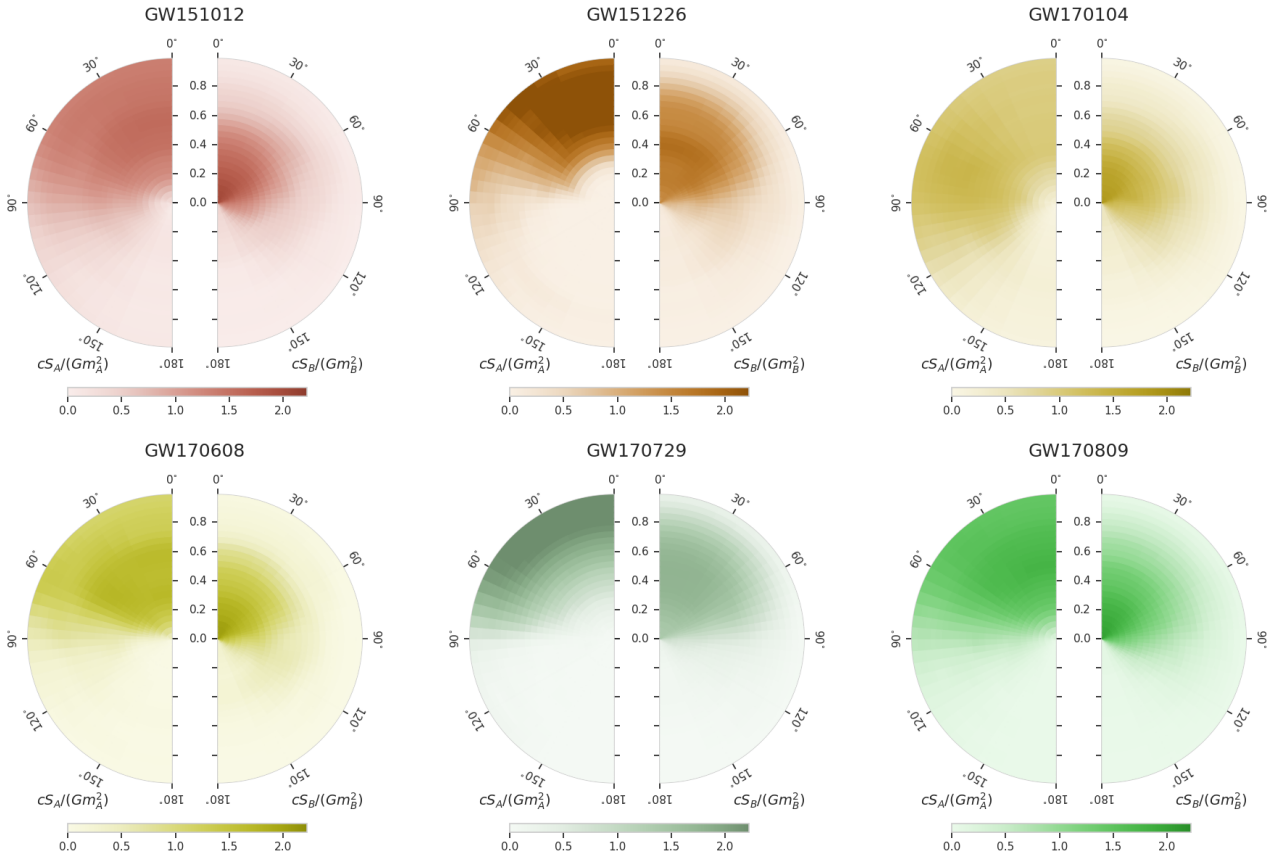

FIG. 7. Spin disk plots for the spin-sorted posterior samples for current LVC detections.

[3] V. Varma, S. E. Field, M. A. Scheel, J. Blackman, D. Gerosa, L. C. Stein, L. E. Kidder, and H. P. Pfeiffer, Phys. Rev. Research. **1**, 033015 (2019), arXiv:1905.09300 [gr-qc].

[4] D. Wysocki, J. Lange, and R. O'Shaughnessy, Phys. Rev. D **100**, 043012 (2019).

[5] B. Abbott *et al.* (LIGO Scientific, Virgo), Astrophys. J. Lett. **882**, L24 (2019), arXiv:1811.12940 [astro-ph.HE].

[6] C. Talbot and E. Thrane, Astrophys. J. **856**, 173 (2018), arXiv:1801.02699 [astro-ph.HE].

[7] C. Talbot and E. Thrane, Phys. Rev. D **96**, 023012 (2017), arXiv:1704.08370 [astro-ph.HE].

[8] T. J. Loredo, in *Bayesian Inference and Maximum Entropy Methods in Science and Engineering ed R. Fischer, R. Preuss and U. V. Toussaint*, AIP Conference Series, Vol. 735 (AIP, Melville, NY, 2004) p. 195.

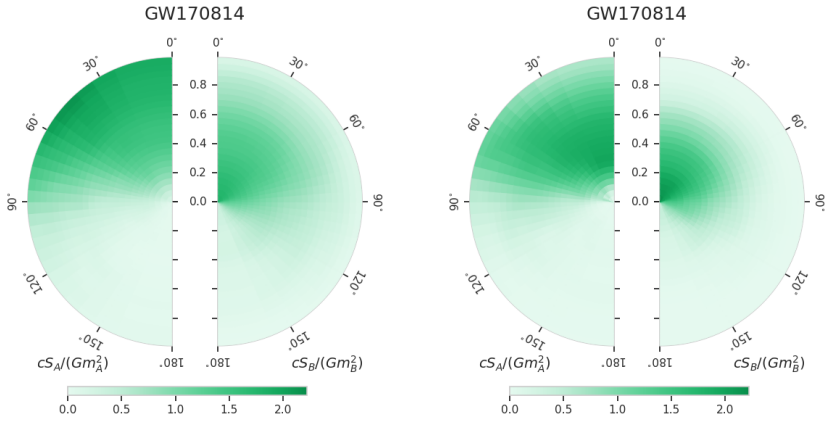

FIG. 8. Spin disk plots for the spin-sorted posterior samples for GW170814 using the IMRPhenomPv2 waveform on the left and the SEOBNRv3 waveform on the right.

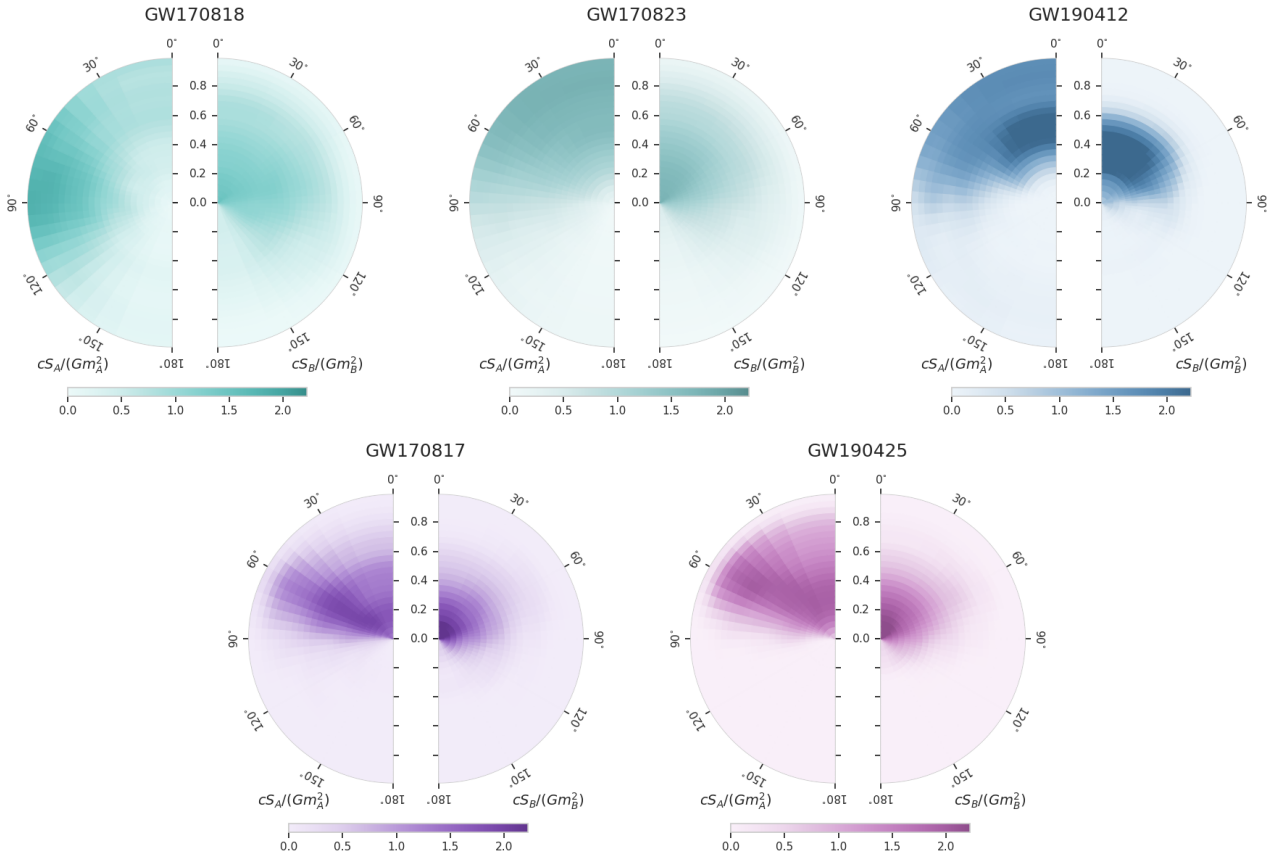

FIG. 9. Spin disk plots for the spin-sorted posterior samples for current LVC detections.

[9] M. Fishbach, D. E. Holz, and W. M. Farr, Astrophys. J. Lett. **863**, L41 (2018).

[10] E. Thrane and C. Talbot, Publ. Astron. Soc. Austral. **36**, e010 (2019), arXiv:1809.02293 [astro-ph.IM].

[11] D. Wysocki, J. Lange, and R. O'Shaughnessy, Phys. Rev. D **100**, 043012 (2019).

[12] I. Mandel, W. M. Farr, and J. R. Gair, MNRAS **486**, 1086 (2019), http://oup.prod.sis.lan/mnras/article-pdf/486/1/1086/28390969/stz896.pdf.

[13] S. Vitale, (2020), arXiv:2007.05579 [astro-ph.IM].

[14] B. Abbott *et al.*, "GWTC-2 Data Release: Sensitivity of Matched Filter Searches to Binary Black Hole Merger Populations," (2020).

[15] R. Abbott *et al.* (LIGO Scientific, Virgo), (2020), arXiv:2010.14527 [gr-qc].

[16] W. M. Farr, Research Notes of the AAS **3**, 66 (2019).

[17] R. Abbott *et al.* (LIGO Scientific, Virgo), (2020), arXiv:2010.14533 [astro-ph.HE].

[18] B. Abbott *et al.* (LIGO Scientific, Virgo), Phys. Rev. X **9**, 031040 (2019), arXiv:1811.12907 [astro-ph.HE].

[19] R. Abbott *et al.* (LIGO Scientific, Virgo), (2019), arXiv:1912.11716 [gr-qc].

[20] B. Abbott *et al.*, "GWTC-2 Data Release: Parameter Estimation Samples and Skymaps," (2020).

[21] J. S. Speagle, MNRAS **493**, 3132 (2020), https://academic.oup.com/mnras/article-pdf/493/3/3132/32890730/staa278.pdf.

[22] C. Talbot, R. Smith, E. Thrane, and G. B. Poole, Phys. Rev. D **100**, 043030 (2019).

[23] S. Husa, S. Khan, M. Hannam, P. Michael, F. Ohme, X. Jiméz Forteza, and A. Bohé, Phys. Rev. D **93**, 044006 (2016), arXiv:1508.07250 [gr-qc].

[24] M. Hannam, P. Schmidt, A. Bohé, L. Haegel, S. Husa, F. Ohme, G. Pratten, and M. Pürrer, Phys. Rev. Lett. **113**, 151101 (2014).

[25] S. Khan, S. Husa, M. Hannam, F. Ohme, P. Michael, X. Jiméz Forteza, and A. Bohé, Phys. Rev. D , 044007 (2016), arXiv:1508.07253 [gr-qc].

[26] S. Babak, A. Taracchini, and A. Buonanno, Phys. Rev. D **95**, 024010 (2017), arXiv:1607.05661 [gr-qc].

[27] A. Taracchini *et al.*, Phys. Rev. D **89**, 061502 (2014), arXiv:1311.2544 [gr-qc].

[28] Y. Pan, A. Buonanno, A. Taracchini, L. E. Kidder, M. H., H. P. Pfeiffer, M. A. Scheel, and B. Szilái, Phys. Rev. D **89**, 084006 (2014), arXiv:1307.6232 [gr-qc].

[29] R. Abbott *et al.* (LIGO Scientific, Virgo), Phys. Rev. D **102**, 043015 (2020), arXiv:2004.08342 [astro-ph.HE].

[30] B. Abbott *et al.* (LIGO Scientific, Virgo), Phys. Rev. Lett. **119**, 161101 (2017), arXiv:1710.05832 [gr-qc].

[31] B. Abbott *et al.* (LIGO Scientific, Virgo), Astrophys. J. Lett. **892**, L3 (2020), arXiv:2001.01761 [astro-ph.HE].

[32] B. Abbott *et al.* (LIGO Scientific, Virgo), Phys. Rev. Lett. **116**, 241102 (2016), arXiv:1602.03840 [gr-qc].

[33] C. Hoy and V. Raymond, (2020), arXiv:2006.06639 [astro-ph.IM].